NTNU
Norwegian University of
Science and Technology

Initial Stages of Metal Dusting Corrosion

Surface and subsurface investigation using
SEM, Raman spectroscopy, and STEM

John Helms

Chemical Engineering
Submission date: June 2018
Supervisor: Hilde Johnsen Venvik, IKP

Norwegian University of Science and Technology
Department of Chemical Engineering

Abstract

Metal dusting (MD) is a corrosion phenomenon that often occurs in industrial processes involving syngas. Carbon deposited on vessel walls gradually causes disintegration of the bulk metal. Because MD is related to carbon deposition, conditions where MD can arise are often described using a thermodynamic parameter called carbon activity (a_c), which describes the likelihood of carbon deposition. MD can occur with $a_c > 1$.

Inconel 601 and Incoloy 800 alloy wafers were treated in two steps. Wafers were first subjected to a 10% steam, 90% argon environment at 650°C for 360 minutes. They were then exposed to a condition with very high a_c ($>>1$): a 10% carbon monoxide 90% argon, 540°C environment for 20, 60, 120, 300, and 1200 minutes in an attempt to induce carbon deposition and metal dusting.

SEM indicated that 601 wafers experienced extensive development of carbon filaments over the whole working wafer surface. Coverage was not as uniform on 800 wafers, but evidence of carbon deposition was found on all wafers. The poor resistance of the 601 wafers to carbon deposition is likely due to the oxidation step not being aggressive enough to form a proper resistant oxide scale. Variation in carbon coverage on 800 wafers could arise from variation in the pre-polishing of the wafers, which was done by hand.

Analysis with Raman spectroscopy suggests that carbon on the surface of the 601 wafers has higher crystallinity than that on the 800 wafers, but there was no obvious trend with different duration of the metal dusting step.

An area on the 60 minute exposed 800 sample was selected for TEM study. A difference in the amount of deposited carbon was identified on either side of a grain boundary. This difference was correlated with the development of a chromium-deficient layer and the

oxide scale layer. A clearer, larger chromium-deficient layer and thicker oxide scale was associated with less carbon deposition on the surface. Carbon filaments were found to contain metal particles and separate them from the surface through growth. SAD indicated a grain orientation difference between the regions. Further Raman analysis was attempted on similar areas of the wafer.

Preface

This thesis is written for completion of the MSc program in Chemical Engineering at the Norwegian University of Science and Technology through the Department of Chemical Engineering. The thesis was written during the Spring semester of 2018, and it accounts for 30 credits.

I would like to thank Hilde J. Venvik for supervision and support of the project and thesis, as well as co-supervisors Xiaoyang Guo and Per Erik Vellum. Estelle Marie M. Vanhaecke also provided invaluable insight and support.

The Research Council of Norway is acknowledged for the support to the Norwegian Micro- and Nano-Fabrication Facility, NorFab, project number 245963/F50.

I certify that this is an independent work in accordance with the exam regulations of NTNU.

Table of Contents

List of Figures

Abbreviations

BF	=	Bright Field
DF	=	Dark Field
EDS	=	Energy dispersive x-ray spectroscopy
EELS	=	Electron energy loss spectroscopy
LFC	=	Liquid flow controller
MD	=	Metal dusting
MFC	=	Mass flow controller
PC	=	Pressure controller
SAD	=	Selected Area Diffraction
SEM	=	Scanning electron microscope
STEM	=	Scanning transmission electron microscope
Syngas	=	Synthesis gas

Chapter 1

Introduction

1.1 Metal Dusting

Metal dusting is a type of corrosion associated with carbon deposition on the surface of metals. At a basic level, graphite growth disintegrates metals into small particles. It is most commonly encountered in the process vessels of synthesis gas (syngas) processes (e.g. hydrogen prodution, ammonia production, and Fischer-Tropsch) [9], but has the potential to occur in most cases where carbon is being deposited on a metal. Syngas is a common chemical precursor that consists mostly of carbon monoxide and hydrogen. Metal dusting is particularly favored between 400 and 800°C at low pressures in syngas processes [10].

Metal dusting has a significant economic impact. A 2007 United States Department of Energy report estimated that alloys with improved metal dusting resistance could have savings in the U.S. hydrogen production industry alone of $1.3 billion [9] each year. Improved understanding of treatments and conditions that reduce the prevalence and rate of metal dusting are therefore desirable.

1.2 Scope of Present Work

The later stages and progression of metal dusting (e.g. pitting and metal wastage) are relatively well described. The early stages of metal dusting just after carbon deposition and the development of carbon filaments have been less studied. Study of these stages could aid in development of resistant alloys and treatments to improve resistance.

The present work focuses on the initial stages of metal dusting with focus paid to oxide scale formation and characterization, the properties of deposited carbon, and possible explanations for observed variation within and between samples.

Scanning electron microscopy is used to characterize sample surface topography and carbon coverage. Raman spectroscopy is used to characterize deposited carbon and the oxide scale layer. Transmission electron microscopy and scanning transmission electron microscopy provide information on carbon filaments and the subsurface conditions that give rise to variation in carbon deposition resistance.

Chapter 2

Literature Review

2.1 Thermodynamics

Tendency for carbon to be deposited from a gas phase is usually described using a parameter called carbon activity (a_c), which is a function of partial pressures and temperature conditions. Metal dusting is associated with a_c greater than 1. The most significant reactions for carbon deposition as it relates to metal dusting are the Boudouard Reaction and the reduction of carbon monoxide with hydrogen[11; 10], because the main carbon-containing constituent in syngas is carbon monoxide. When hydrocarbons are present in large amounts, alkane cracking and methane decomposition may also contribute to carbon deposition[10].

The Boudouard reaction is:

$$2CO_{(g)} <-> C_{(s)} + CO_2$$

$$\Delta H^{\circ}_{298} = -172.4kJ/mol$$

The CO reduction reaction is:

$$CO_{(g)} + H_{2(g)} <-> C_{(s)} + H_2O_{(g)}$$

$$\Delta H^{\circ}_{298} = -131.3kJ/mol$$

Both these reactions are exothermic and are thermodynamically favored at low temperatures, but interplay with kinetics means that carbon deposition in syngas processes occurs in the range of 400-800°C [10]. Gas conditions used in experiments in this study have $a_c >> 1$ [11].

2.2 Mechanism

In iron-based alloys, Grabke suggests the following mechanism:

1. Carbon transfers into metal phase and oversaturates.

2. Fe_3C and Ni_3C form at surface and prevent further transfer of carbon into the alloy.

3. Graphite precipitates and destabilizes the carbides, which decompose back to the metallic form.

4. Carbon atoms grow into cementite and the metals agglomerate.

5. Metal agglomerates catalyze coke deposition.

For alloys with high chromium content, which tend to form a protective scale, he suggests a slighly different mechanism:

1.Local defects form in the oxide scale, which allow dissolution of carbon into the metal phase.

2. Carbon diffuses into metal and forms carbide precipitates.

3. Carbon activity rises to >1.

4. Disintegration begins via formation of cementite (and volume expansion) and internal growth of graphite.[1]

5. Agglomerated metal particles catalyze carbon deposition (coking).

This mechanism is represented in Figure 2.1, which is included because the alloys studied in this thesis form Cr-rich oxide scales.

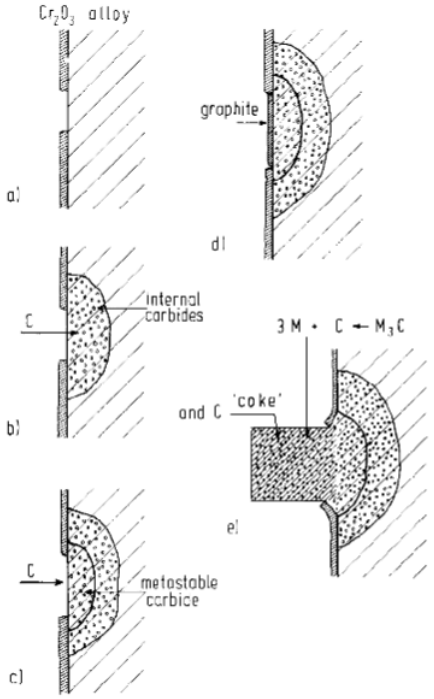

Figure 2.1: Proposed mechanism for metal dusting in Cr-rich alloys [1].

It has been observed that metal dusting is always accompanied by carbon filamentation [3]. Zeng et al further suggest that the lattice planes of metals and cementites catalyze carbon formation by serving as templates that allow higher crystallinity and lower free energy carbon to form 3; 2. This is depicted in Figure 2.2. Zeng suggests that carbon filamentation plays a more active role in metal dusting by dispersing dusted metal particles.

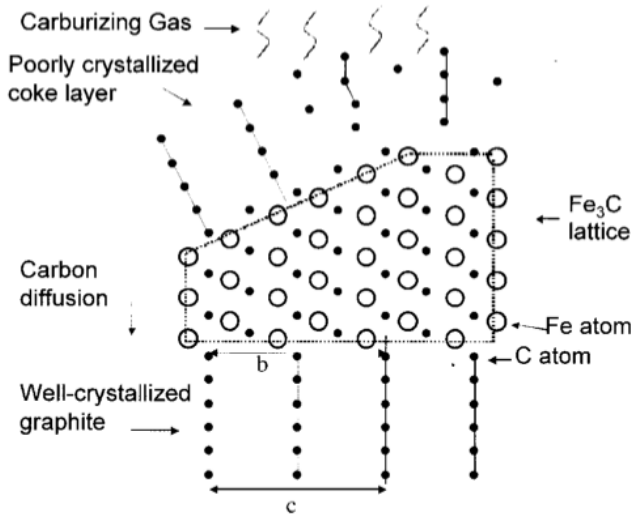

Fig. 20. Poorly crystallized carbon dissolves in and diffuses through cementite, whose lattice provides excellent orientation for crystallization of graphite; *b* dimension of cementite (6.743 Å) is very close to *c* dimension of graphite (6.724 Å).

Figure 2.2: Depiction of catalytic recrystallization of carbon as it passes through the cementite lattice [2].

This is shown in Figure 2.3

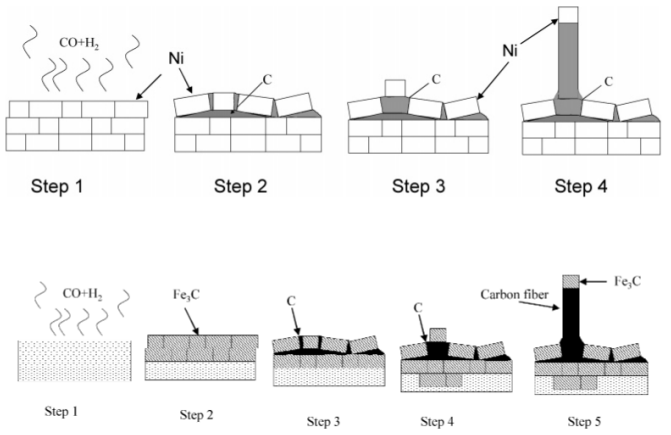

Figure 2.3: Proposed mechanism for carbon growth and disintegration of carbon via carbon filament formation in nickel (top) and iron (bottom) based alloys [3].

2.3 Oxide scaling and metal dusting inhibition

The characteristics of the oxide formed on the surface of the alloy play a critical factor in the extent of metal dusting. Zeng et al found that oxide scales high in Cr_2O_3 and $FeCr_2O_4$ greatly inhibit metal dusting due to significantly higher activation energy of carbon deposition, while some spinels that may form in the oxide layer may actually catalyze carbon deposition [12]. Metal dusting will begin as soon as there are cracks in a chromium-rich oxide layer that expose the underlying bulk; these cracks may arise from internal stress in the oxide layer or from stress caused by metal-dusting in a non-chromium rich area [13; 14].

Grabke suggests that high alloy steels are highly susceptible to metal dusting in the temperature range 500-650°C compared to >650°because no chromium rich oxide scale is formed at the lower temperatures[1].

Grinding of an alloy surface subjected to metal dusting conditions can improve resistance by creating many dislocations which increase the rate of chromium diffusion and resistant scale formation [1]. Oxide scale composition can be correlated with tarnish color and differences in carbon deposition have been seen on different-colored grains of alloy 800 [15].

2.4 Grain dependence

Grain orientation plays a role in oxide scale formation and therefore affects carbon deposition and metal dusting. Low-index grains on alloy 800 (e.g. (001)) have been seen to be more resistant to metal-dusting [15].

2.5 Carbon crystallization

Due to the previously suggested mechanism of catalyzed recrystallization of carbon, carbon filaments that are produced during the metal dusting process should have higher crystallinity than carbon deposited as coke on the surface. Researchers have shown this via Raman spectroscopy through analysis of the D (disordered) and G (graphitic) bands of carbon and have further found that carbon located inside pits caused by metal dusting have higher crystallinity than those outside[16; 3]. This is shown in Figure 2.4. Other

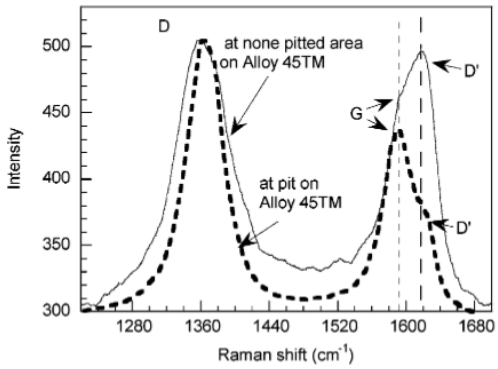

Figure 2.4: Comparison of Raman spectroscopy carbon bands inside and outside metal dusting pits on an alloy [3].

researchers have attempted to further deconvolute carbon bands appearing in Raman spectroscopy to five peaks:

D1: associated with defects in graphite lattice edges

G: graphitic lattice vibrations

D2: defects in surface graphene layers

D3: amorphous sp^2 carbon forms

D4: sp^2-sp^3 bonds or C-C/C=C bond stretching[4; 17]

The peaks and their characteristic positions are shown in Figure 2.5. Comparing ratios

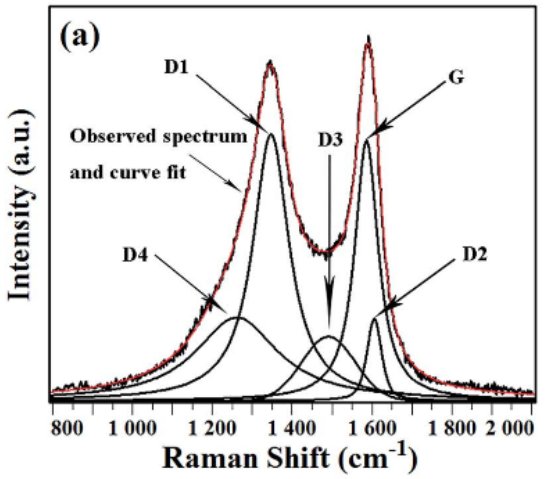

Figure 2.5: Deconvolution of Raman spectrum into five carbon peaks [4].

of peak intensities can provide more information about the crystallinity of carbon and a more accurate G/D1 ratio since the D2 peak always appears as a shoulder on the G peak [4].

Chapter 3

Materials and Methods

3.1 Alloy Wafers

Inconel 601 and Incoloy 800 are high-performance alloys used in industrial vessels and tubing. Inconel 601 is composed of 58-63% nickel, 21-25% chromium, 20-25%, <2% aluminum, and traces (<1%) of copper, silicon, manganese, sulfur, and carbon [18]. Incoloy 800 is composed of 30-35% nickel, 19-23% chromium, 39.5% iron, and trace (<0.6%) amounts of titanium and aluminum [19]. Both alloys are selected for use in environments where high chemical resistance is required. Manufacturer data sheets suggest Inconel 601 to be more resistant to carburization due to higher nickel content and lower iron content, with both alloys being significantly more resistant than conventional stainless steel alloys [19]. Alloy wafers measured approximately 15 mm x 8mm and were approximately 0.5 mm thick.

3.2 Experimental set-up

During each experiment, two wafers are suspended from quartz rods hanging from a nut at the top of a vertical tubular reactor with interior gold-plating. This setup is diagrammed in detail in Figure 3.1. The reactor is surrounded by a furnace and insulation, and thermally

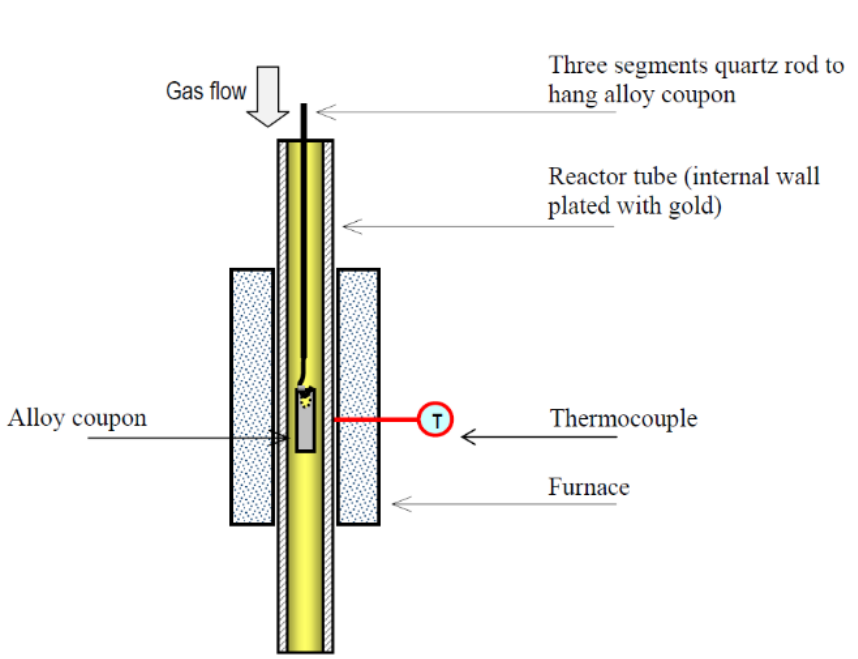

Figure 3.1: A cutaway look at alloy coupons suspended in the experimental reactor

regulated using a type-K thermocouple and a temperature controller (TC) in contact with the exterior reactor wall. Steam is supplied to the reactor from an upstream evaporator at 1 bar and 250°C. Water flow to the evaporator is regulated using a liquid flow controller (LFC) set to supply a volumetric flow corresponding to the desired process steam flow (in the case of this project, 10 ml/min). Steam and other process gases are blended prior to entering the reactor. System pressure is regulated to 1 bar via a pressure controller (PC) on the reactor outlet. A simplified experimental scheme is shown below in Figure 3.2. A detailed diagram of the experimental setup can be found in the Appendix in Figure 6.1.

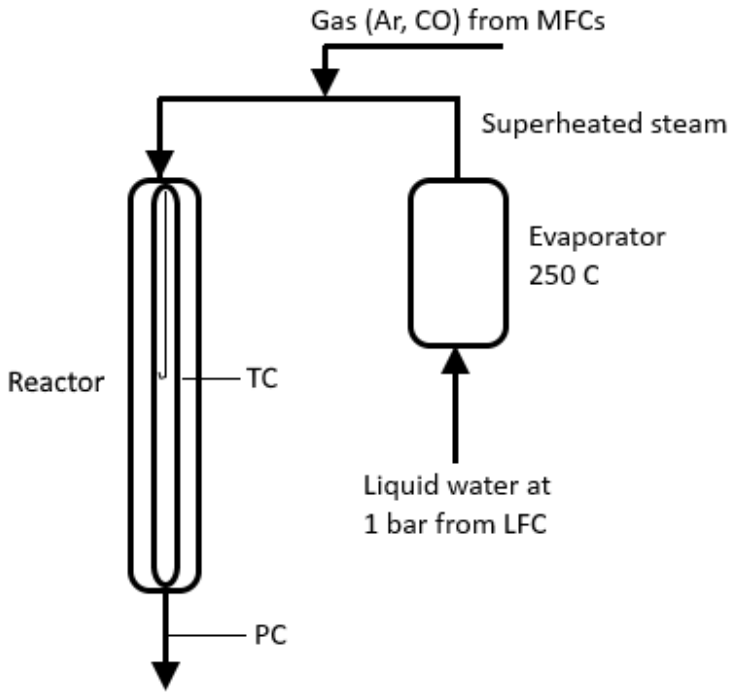

Figure 3.2: A simplified experimental setup with key elements.

3.3 Sample Preparation

One side of each sample wafer was ground progressively with SiC polishing paper down to P2500 grit (10 micrometers). Samples were then polished with diamond polishing paste at 6, 3, and 1 micrometers. Previous works 11 indicated that time after polishing could influence carbon formation, so samples were re-polished the day before experimental runs at 3 and 1 micrometers. The wafers were then ultrasonicated for 30 minutes in acetone and then in hexane before being left to dry overnight.

3.4 Characterization Techniques

The main techniques used in this analysis are scanning electron microscopy (SEM), transmission electron microscopy/scanning transmission electron microscopy (TEM/STEM), and Raman spectroscopy.

3.4.1 Scanning electron microscopy

Scanning electron microscopy is used for analyzing surface topography. In SEM, a focused beam of electrons is scanned across the surface of a bulk material. The characteristics of re-emitted electrons recorded by detectors are used to construct an image of the surface or otherwise analyze composition. Images and analyses are constructed pixel-by-pixel in a manner similar to cathode ray tube television, hence ”scanning” electron microscopy[7]. Because SEM relies on electrons re-emitted from the bulk (and in the primary case, secondary electrons), images of non-homogeneous samples may exhibit features that are actually subsurface [5]. Caution must be used when interpreting these images. The different types of interactions of the sample with the electron beam are shown in Figure 3.3.

The penetration depth and interaction volume of the electron probe depend on the composition - electrons penetrate farther into samples composed of low atomic number elements - and device parameters such as beam current [5]. The electron interactions and scattering at different relative depths of the sample and an illustration of interaction volume is shown in Figure 3.5.

3.4.2 Transmission electron microscopy and scanning transmission electron microscopy

In transmission electron microscopy, a beam of electrons is passed through a thin ($<$50 nm) sample. Transmitted electrons are used to construct an image of the sample. Scanning

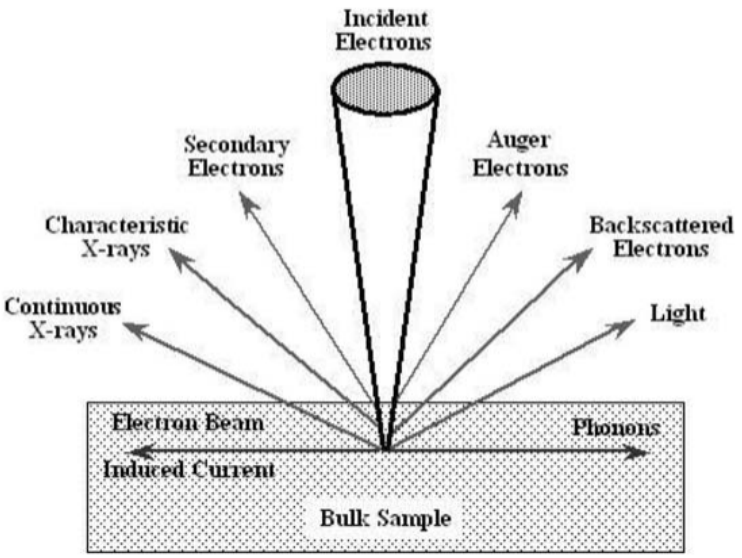

Figure 3.3: The different types of interactions of the SEM electron beam with the bulk material[5].

transmission electron microscopy incorporates a similar image construction technique as in SEM - a 1-10 angstrom electron beam is swept across the sample, and an image is constructed pixel-by-pixel [7]. The general schemes and electron paths of TEM, SEM, and STEM are shown in Figure 3.4. Energy dispersive x-ray spectroscopy (EDS) and electron energy loss spectrometry (EELS) can be performed at each pixel location to provide information on elemental composition in that area[6]. In EDS, an x-ray spectrum allows determination of elemental concentration. EELS measures energy loss of electrons transmitted through the sample, which can provide information about sample composition and structure at that point [7]. Both Bright Field images (i.e. constructed of undiffracted transmitted electrons) and Dark Field images (constructed from diffracted electrons) can be obtained [7]. Figure 3.5 illustrates the difference in interaction volumes between SEM and TEM. TEM interaction volume is determined by the width of the incident electron beam.

TEM is used in this thesis to examine a cross-section of a surface that was identified using SEM. In this way, TEM can provide information on the sub-surface phenomena that is impossible to obtain with SEM. Non-homogeneity and variations in sample thickness

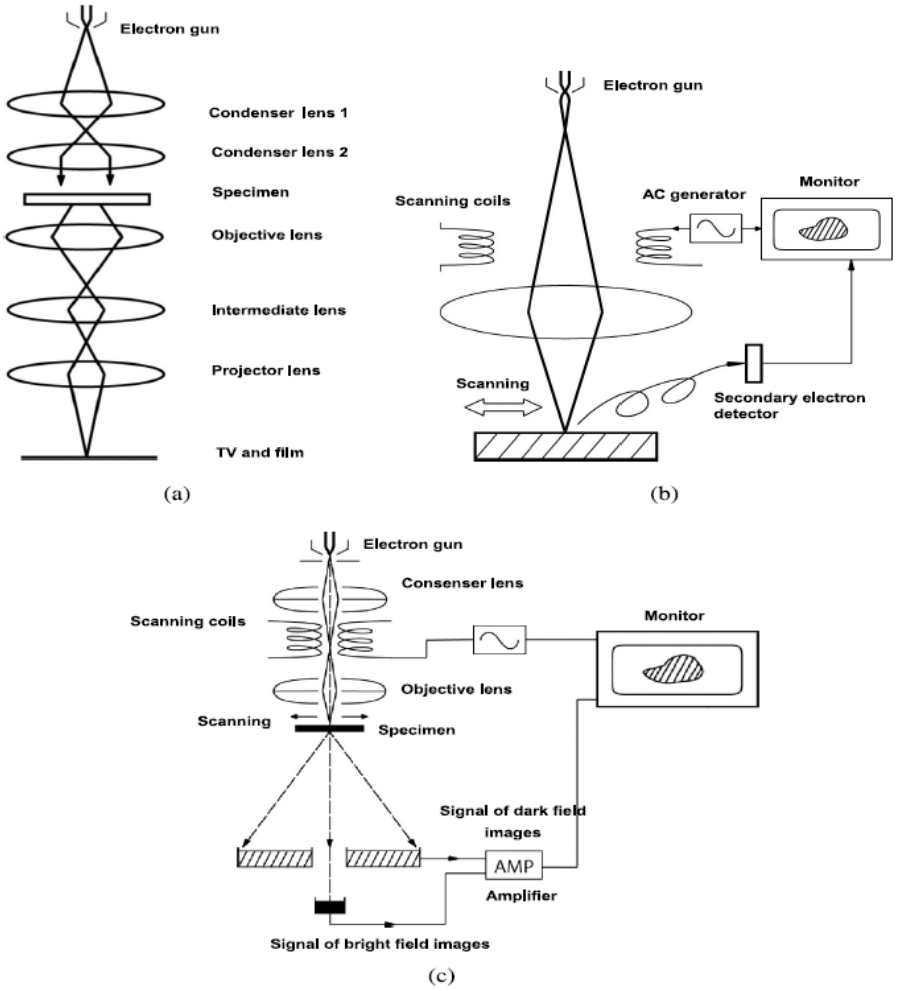

Figure 3.4: Simplified schemes and electron paths of (a) TEM, (b) SEM, and (c) STEM [6].

are a concern because information from the whole thickness of the sample goes into the constructed image. Further, the small interaction volume and size of the sample poses the risk for non-homogeneous samples that the analyzed area is not characteristic of the bulk sample.

Focused Ion Beam (FIB) was used to create the cross-section of an area of interest identified using SEM. The transmission electron microscope used in this work is a Jeol JEM ARM200F Double-corrected ColdFEG TEM.

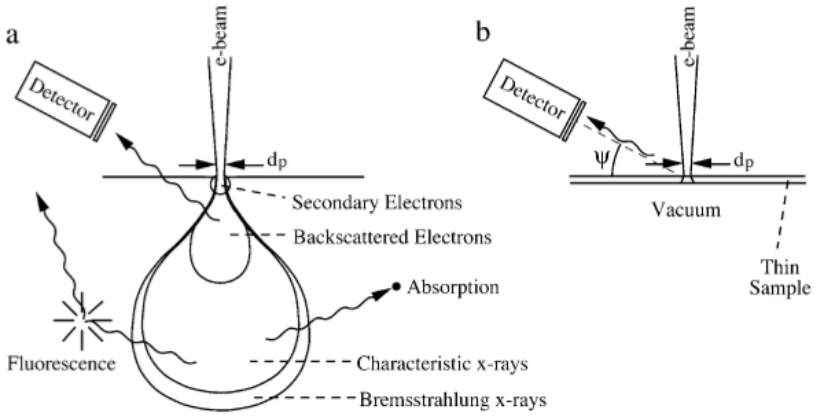

Figure 3.5: SEM and TEM electron interaction volumes[7].

3.4.3 Raman

Raman spectroscopy is used to identify molecules on the surface of the alloy wafers. In Raman spectroscopy a sample is exposed to a monochromatic light source, such as a laser. Incident photons interact with the sample, cause a vibrational excitation, and are inelastically scattered as photons with reduced frequency. This is a phenomenon known as Raman scattering. Different molecules have characteristic frequencies that are determined empirically or using mathematical calculations and group theory 8. The light source used was a red laser with wavelength of 533 nm. 50x and 100x magnifications were used.

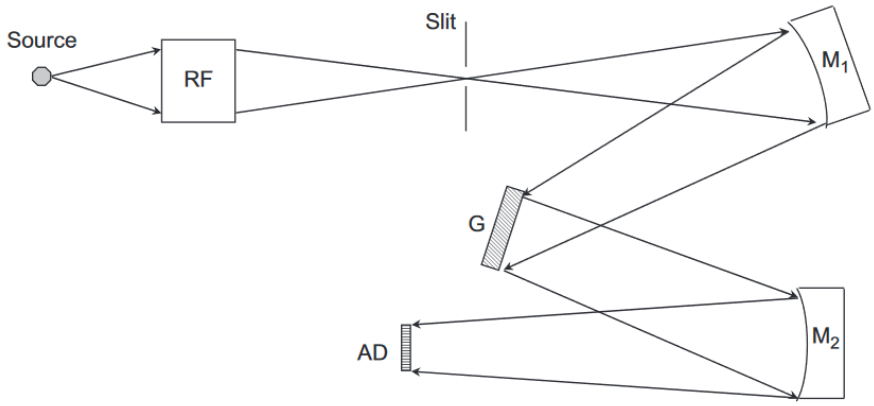

Figure 3.6: Generalized Raman spectrometer set-up. The source is the sample surface, RF is a Rayleigh filter to remove elastically scattered light, M1 and M2 are mirrors, G is a grating, and AD is the array detector [8].

Chapter 4

Experiment

Experiments involved one wafer of each of the studied alloys (Inconel 601 and Incolloy 800). After the polishing and cleaning procedure described previously, wafers were loaded into the reactor. The reactor was then pressurized to 5 bar using argon and left overnight to check for leaks. Pressure in the reactor is then reduced to 1 bar, at which all experiments are carried out. Wafers were then subjected to a flow of 10 mL/min steam, 90 mL/min argon for 360 minutes at 540°C as a pre-oxidation step. After 360 minutes had elapsed, water flow was cut off and the samples were exposed only to argon. After purging for 1 minute, the temperature controllers began to ramp at 10°C/min until the setpoint for the metal dusting condition was reached.

The total duration of the intermediate step between oxidation and metal dusting treatments was 30 minutes. Then, wafers were exposed to a flow of carbon monoxide at 10 mL/min and argon at 90 mL/min at 650°C as the metal dusting step. Experiments were performed with metal dusting steps lasting 20, 60, 120, 300, and 1200 minutes. After the metal dusting step had elapsed, carbon monoxide flow was turned off and wafers were subjected to only argon until the setup had cooled enough to allow removal.

An additional experiment was performed using 750°C for both the oxidation and metal

dusting steps with a 360 minute oxidation step and a 1200 minute metal dusting step. All other conditions were kept the same as the other experiments. This experiment is used in this thesis to examine oxide formation in Inconel 601.

Chapter 5

Results and Analysis

5.1 SEM

SEM micrographs for each metal dusting condition sample were acquired at various magnifications. A time series of all samples at 30000x magnification is shown in Figure 5.1. Inconel 601 showed extensive carbon deposition for every metal dusting time condition with consistent coverage over the whole working surface of the ally. Only for the 20 minute exposure can features other than carbon filaments be discerned; parts of the oxide layer can be seen sticking up from the surface. Incoloy 800 samples showed more variation, with carbon coverage being nonuniform. See, for example, the 1200 minute exposed sample, which shows only partial coverage.

On the Incoloy 800 sample exposed to metal dusting conditions for 60 minutes, no obvious (long) carbon filaments were found, but possible early stages of filaments were found. A micrograph at 100000x magnification is shown in Figure 5.2 showing some possible filaments. EDS confirmed that these features were carbon, and carbon peaks appeared in Raman spectroscopy. An area on the alloy 800 60 minute metal dusting exposed wafer was selected for TEM study, which will be discussed later.

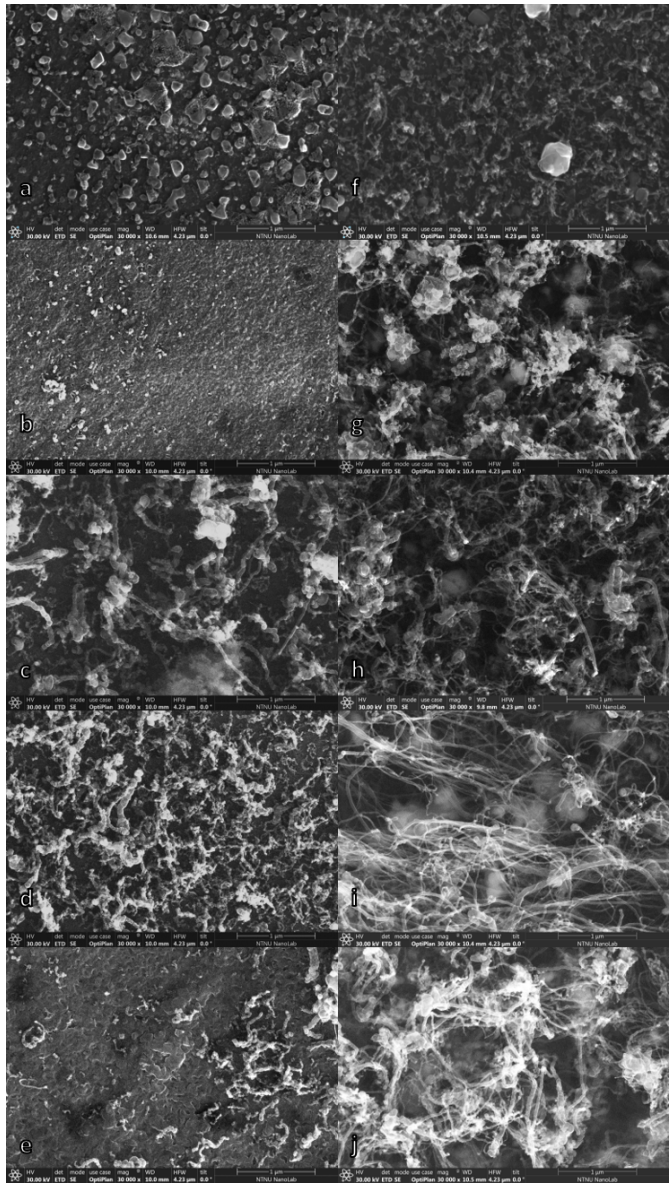

Figure 5.1: Time series of SEM micrographs of the examined metal dusting exposure times. Incoloy 800 is shown on the left side (a-e) (20 min, 60 min, 120 min, 300 min, 1200 min respectively). Inconel 601 is shown on the right side (f-j) (20 min, 60 min, 120 min, 300 min, 1200 min respectively)

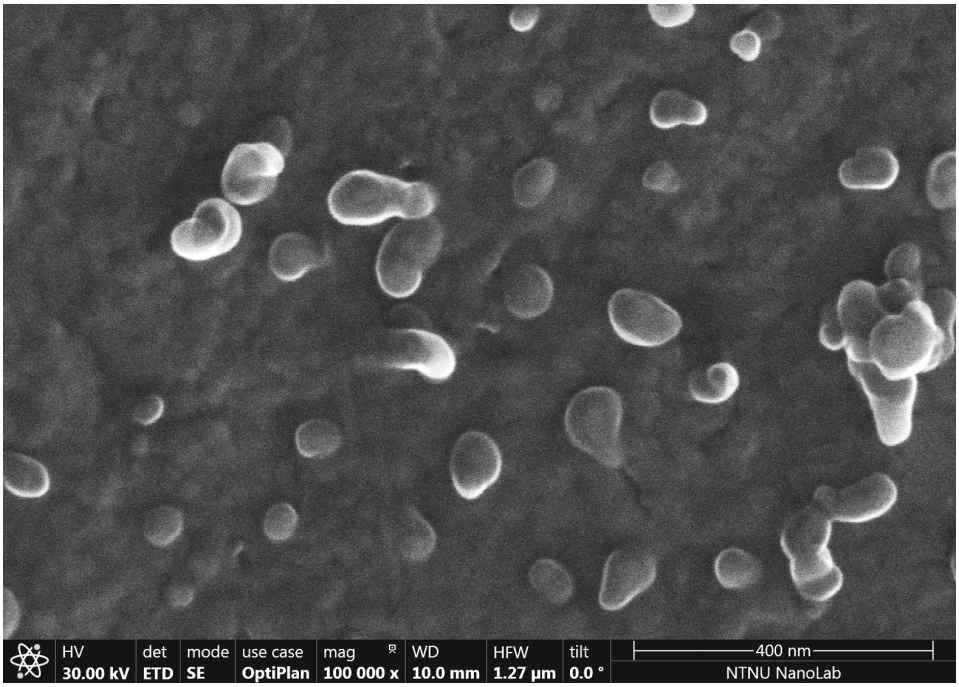

Figure 5.2: SEM image of 60 minute MD exposure 800 wafer showing beginning of carbon filamentation at 100000x magnification

5.2 Raman

Time series were constructed showing normalized characteristic Raman spectroscopy data at each metal dusting condition (20, 60, 120, 300, and 1200 minutes) and for each of the alloys. Inconel 601 data are shown in Figure 5.3, while Incoloy 800 data are shown in Figure 5.4.

The region between 300 cm^{-1} and 750 cm^{-1} has peaks that correspond with various oxides. The largest peak in this region around 650 cm corresponds to spinel 4. Relative comparison of these peaks on Incoloy 800 (Figure 5.4) between MD time conditions suggests that alloy wafers experienced variation in the extent and thickness of oxide formation, with the 60 minute condition having formed the most extensive oxide scale during the pre-oxidation step. This is further supported by the two apparent peaks that appear between 1250 cm^{-1} and 1750 cm^{-1}. These peaks correspond with signals from carbon on the surface of the

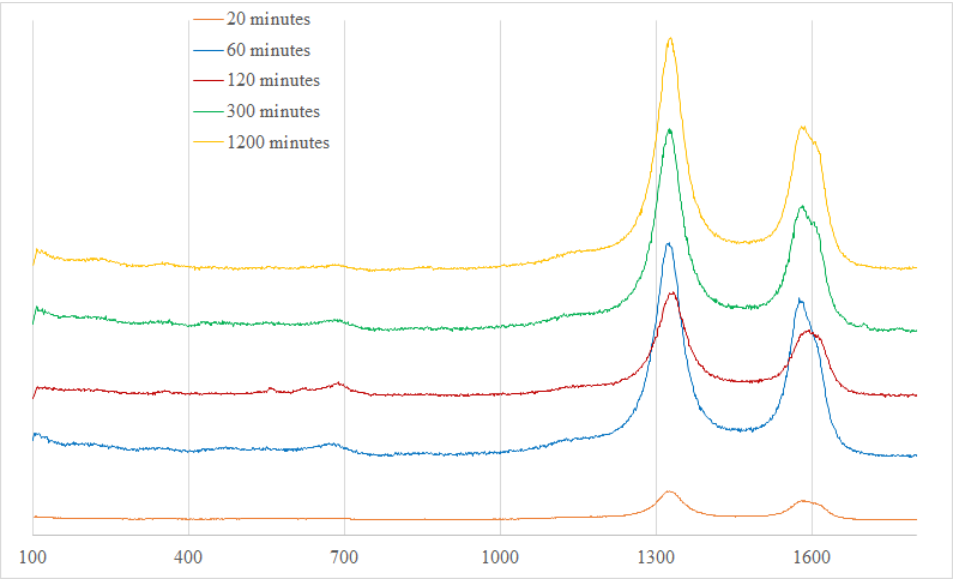

Figure 5.3: Time series by metal dusting exposure times of Raman spectroscopy data for Inconel 601. x-axis: Raman shift, cm^{-1}, y-axis: Arbitrary intensity units

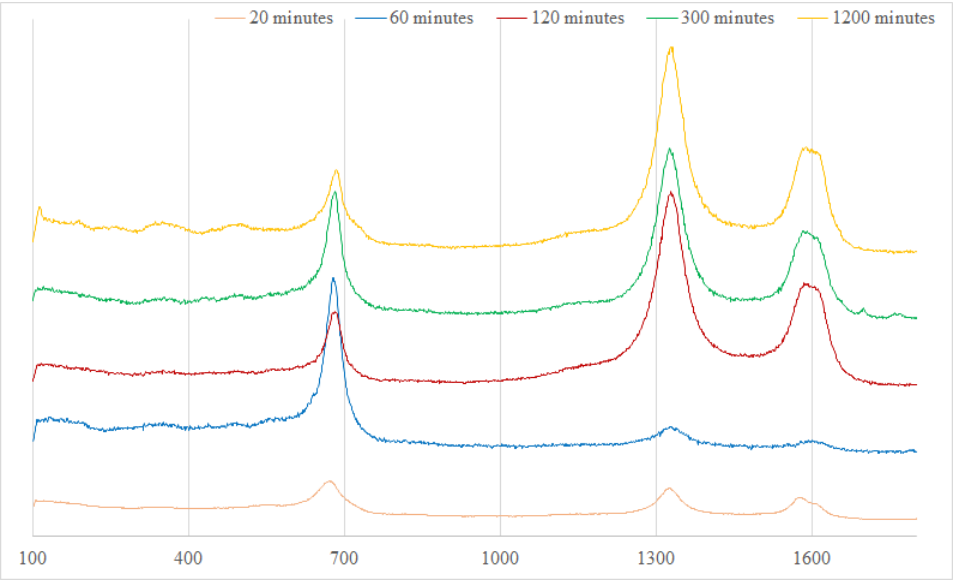

Figure 5.4: Time series by metal dusting exposure times of Raman spectroscopy data for Incoloy 800. x-axis: Raman shift, cm^{-1}, y-axis: Arbitrary intensity units

alloy; the 60 minute sample has the lowest relative intensity of carbon out of all conditions.

These observations match with the previously discussed suppression of carbon deposition by the presence of a well-developed oxide scale. Every wafer in this study experienced the same oxidation condition (360 minutes of 10% steam at 540°C), so the variation in oxide scale formation probably arises from some other processing step, the most likely of which is polishing. Polishing is done by hand and by eye before each experimental run, which opens up the possibility that there are differences in the quality and extent of polishing on each wafer. As discussed previously, polishing/grinding has been seen to significantly impact oxide scale formation, with ground samples showing more resistance to surface carbon deposition [1].

The time series of Inconel 601 shows minimal peaks in the region where oxides should appear (300-750 cm^{-1}). Since none of the conditions exhibit a significant oxide signal and the laser penetration depth is more than the thickness of the carbon filament layer, it is likely that the oxidation temperature was not aggressive enough for formation of a consistent oxide scale as is suggested by Grabke [1]. SEM images show extensive carbon filamentation over the whole alloy surface for Inconel 601 samples, which supports this suggestion.

An experiment was carried out with an oxidation condition of 750°C, 10% steam for 360 minutes followed by metal dusting conditions of 750°C, 10% CO for 1200 minutes. Raman spectroscopy data for the Inconel 601 sample in this experiment is shown in Figure 5.5. The formed oxide shows strong peaks for $MnCr_2O_4$, Cr_2O_3, and $FeCr_2O_4$ between 400 and 650 cm^{-1}, which have higher intensity than the spinel peak found around 700 cm^{-1}[4]. High chromium content oxides are desired to prevent carbon deposition (rather than lower content spinel) [1], and this result suggests that the oxidation condition in the initial experiment was not effective in forming an oxide scale on Inconel 601.

LabSpec6 software was used to perform peak deconvolution as described by Liu et al [4]. An image of the software with an example of the peak fitting and deconvolution is shown in Figure 5.6. Figures showing the ratios of the G peak to all other carbon

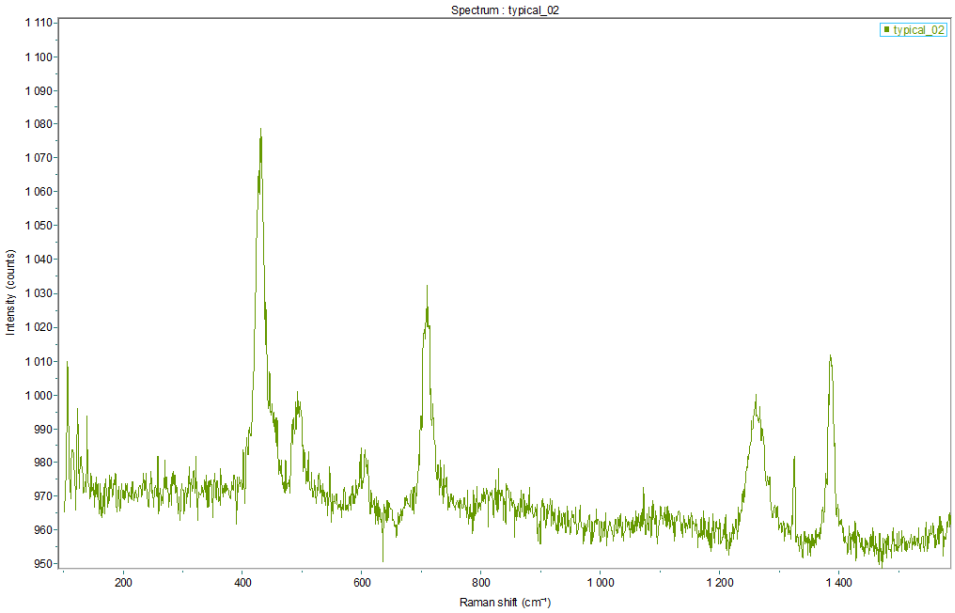

Figure 5.5: Raman spectroscopy data for Inconel 601 sample subjected to 360 minute, 750°C, 10% steam oxidation step followed by 1200 minutes of 10% CO, 750°C metal dusting condition

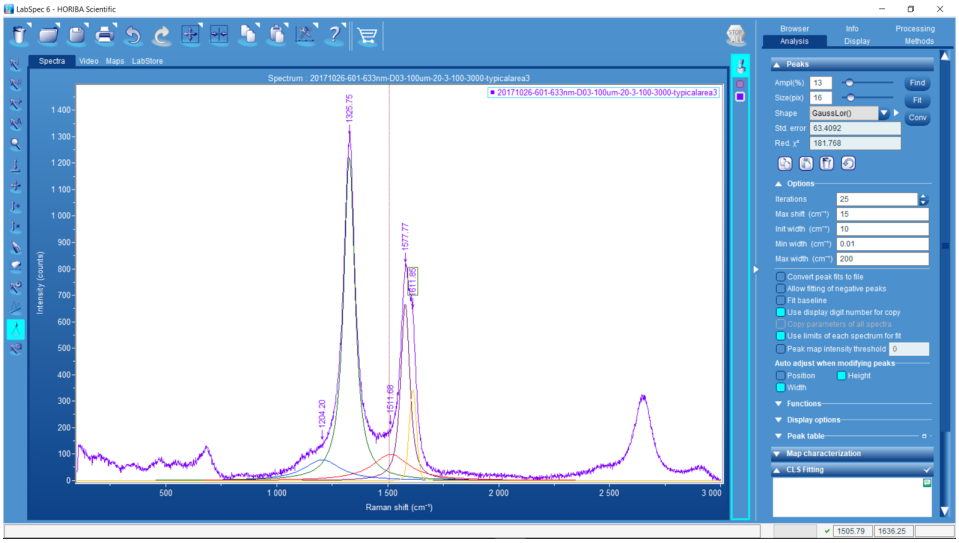

Figure 5.6: Image of the LabSpec6 software and example peak deconvolution

peaks, the D1 peak to the G peak, and the D3 peak to the G peak are shown in Figures 5.7, 5.8, and 5.9, respectively. The G/All ratio is a measure of overall graphitization,

D1/G indicates the degree of carbon structural order (lower is more structured), and D3/G provides information about abundance of amorphous carbon (higher ratios indicate more amorphous carbon). Raman spectroscopy data from at least five points on each wafer was used to calculate an average ratio, which is what is shown in the chart.

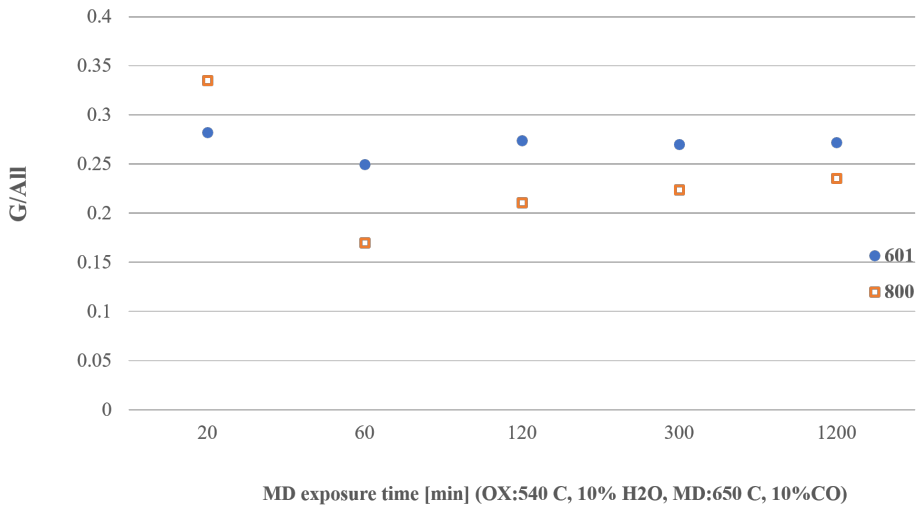

Figure 5.7: Ratio of G peak and all D peaks for each time condition and alloy. Indicates overall degree of graphitization.

Inconel 601 shows high consistency in G/All ratio across all MD time conditions, and is higher than Incoloy 800 at all values other than 20 minutes. This is suggestive of higher rates of carbon deposition and metal dusting due to the previously discussed catalytic recrystallization process that carbon goes through that leads to more graphitic forms of carbon. Likewise, the D1/G and D3/G indicate that the 601 samples generally have more structured carbon and less amorphous carbon, which is also consistent with the enhanced crystallinity of carbon due to metal dusting.

Caution should be used in interpreting this data. Since the peaks are overlapping, small changes in peak locations (a few cm^{-1}) lead to significant changes in deconvoluted peak amplitudes. Small shifts to the left or right of the real peak location can lead to significantly erroneous peak ratios. This also means that the error in the ratios is difficult to quantify - statistical error could have been included in the figures, but that would imply a level

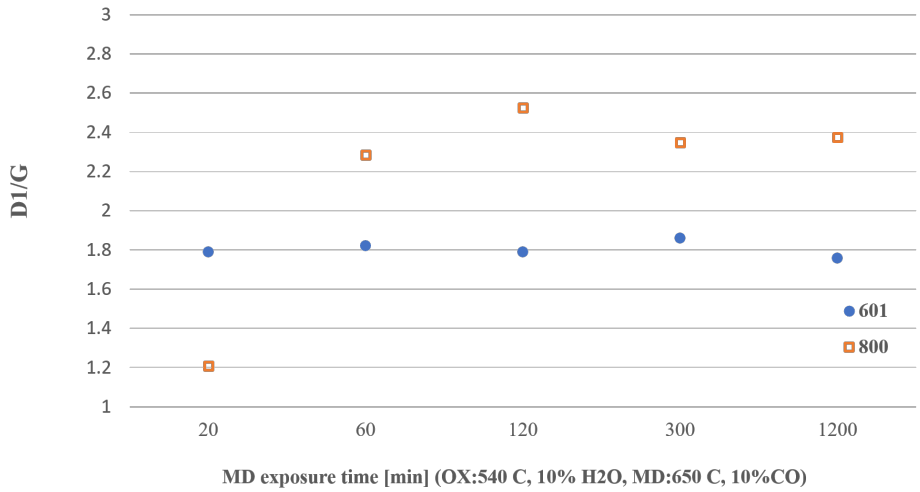

Figure 5.8: Ratio of deconvoluted D_1 peak and G peak for each time condition and alloy. Indicates degree of carbon structural order (lower is more structured).

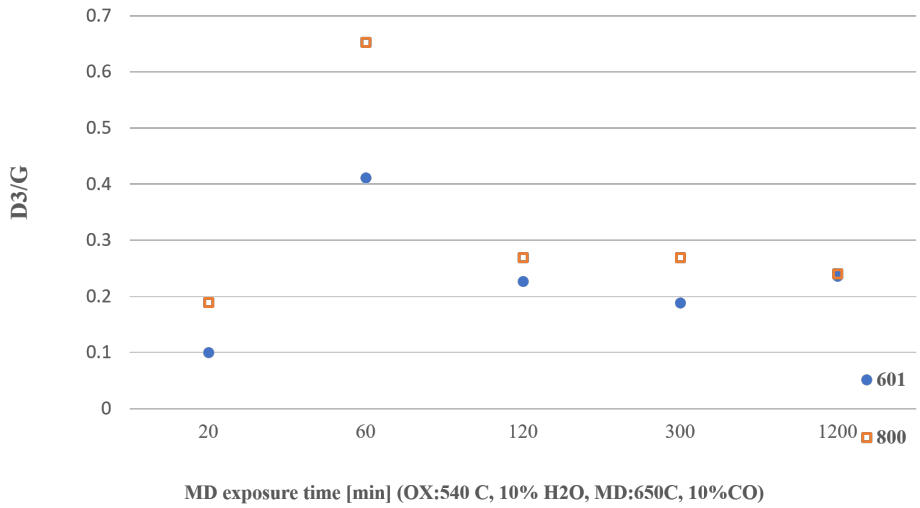

Figure 5.9: Ratio of deconvoluted D_3 peak and G peak for each time condition and alloy. Higher values indicate presence of more amorphous carbon

of confidence in the ratios that is lacking as it would not include the uncertainty in peak deconvolution.

5.3 TEM

An area on the sample of Incoloy 800 that was subjected to 60 minutes of the metal dusting condition was selected for analysis with TEM. The selected area is shown in Figure 5.10. The white box is the targeted area for creation of a thin cross-section with a Focused Ion Beam (FIB). The white dots on the left side of the area were identified as carbon by EDS, while the right side of the box showed much sparser carbon signals.

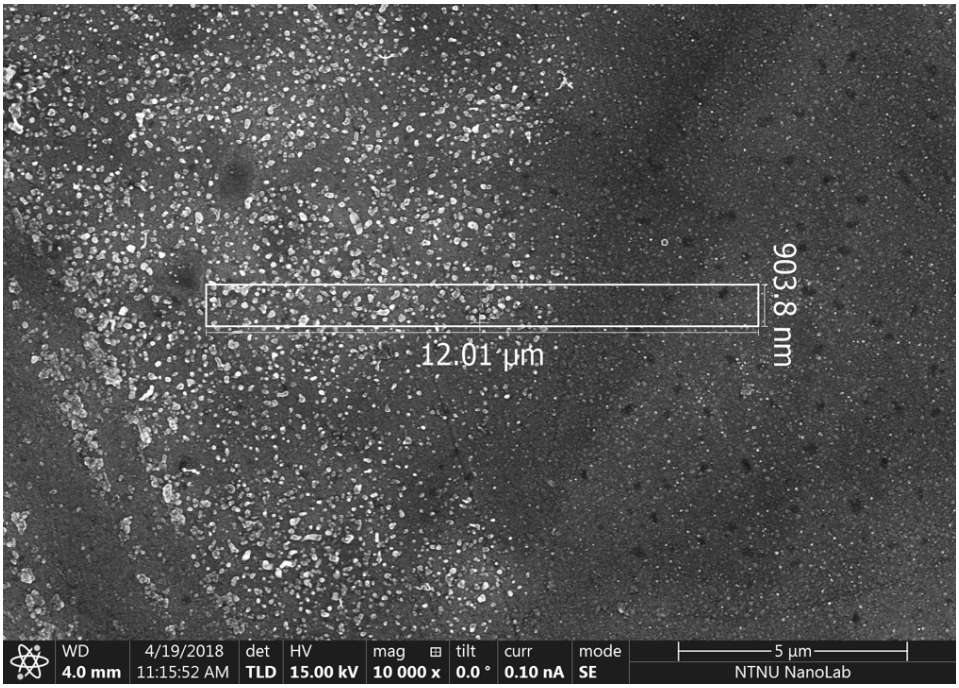

Figure 5.10: SEM micrograph of area on 60 minute MD Incoloy 800 wafer selected for TEM study

An SEM micrograph captured during the sample preparation is shown in Figure 5.11. The micrograph, taken from an angle, shows clear grain boundaries in the bulk material, and seemingly shows that the border between the high carbon coverage and low carbon coverage regions on the surface corresponds with a grain boundary. The right side of the sample is the low carbon coverage region of the sample, while the left side has higher carbon coverage.

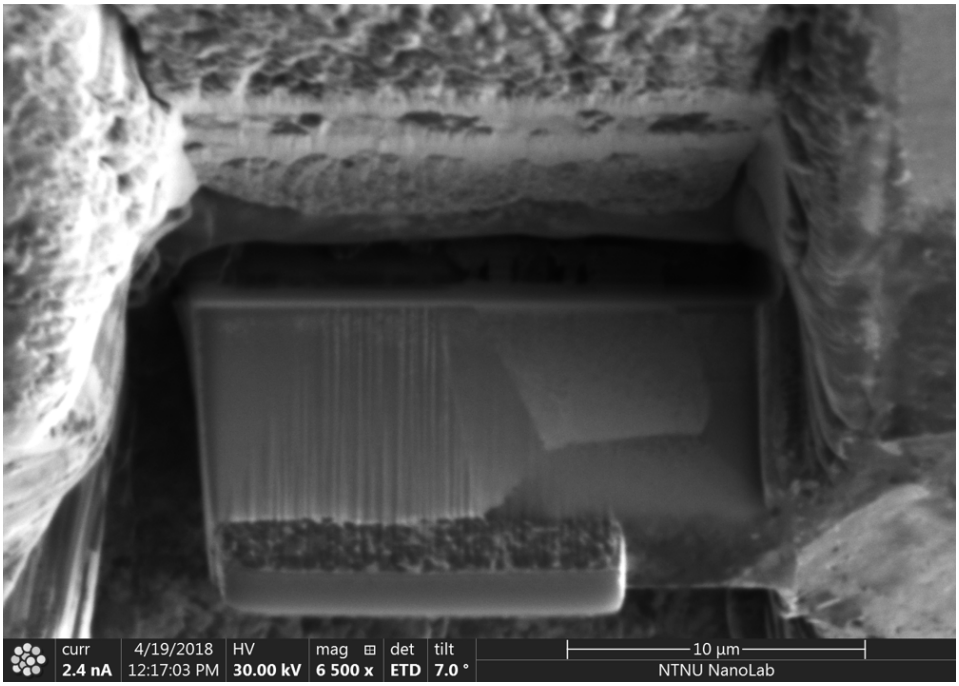

Figure 5.11: SEM micrograph of area of interest during preparation of TEM sample

Figure 5.12 shows an overview TEM image of the sample cross-section. The top right of the image shows the low carbon coverage region. It can already be seen from this image that the area left of the grain boundary (high carbon coverage) has metal particles suspended above the surface (the small black dots in the white layer above the alloy surface).

Figures 5.13, 5.14 and 5.15 show higher magnification images of these suspended particles. Carbon can be seen surrounding the metal particles (the light, stacked layers surrounding the darker metal particles) and separating them from the surface through growth. Thickness of the carbon layer on some of these particles can be seen to be approximately 25 nanometers. Some metal particles have fully separated from the surface, while others are still in the process of separation.

Areas of carbon deposition and metal dusting can also be located on the side of the grain boundary with lower carbon coverage. Carbon-surrounded particles occur with less frequency, and the extent of carbon deposition is much less. Some of these particles are

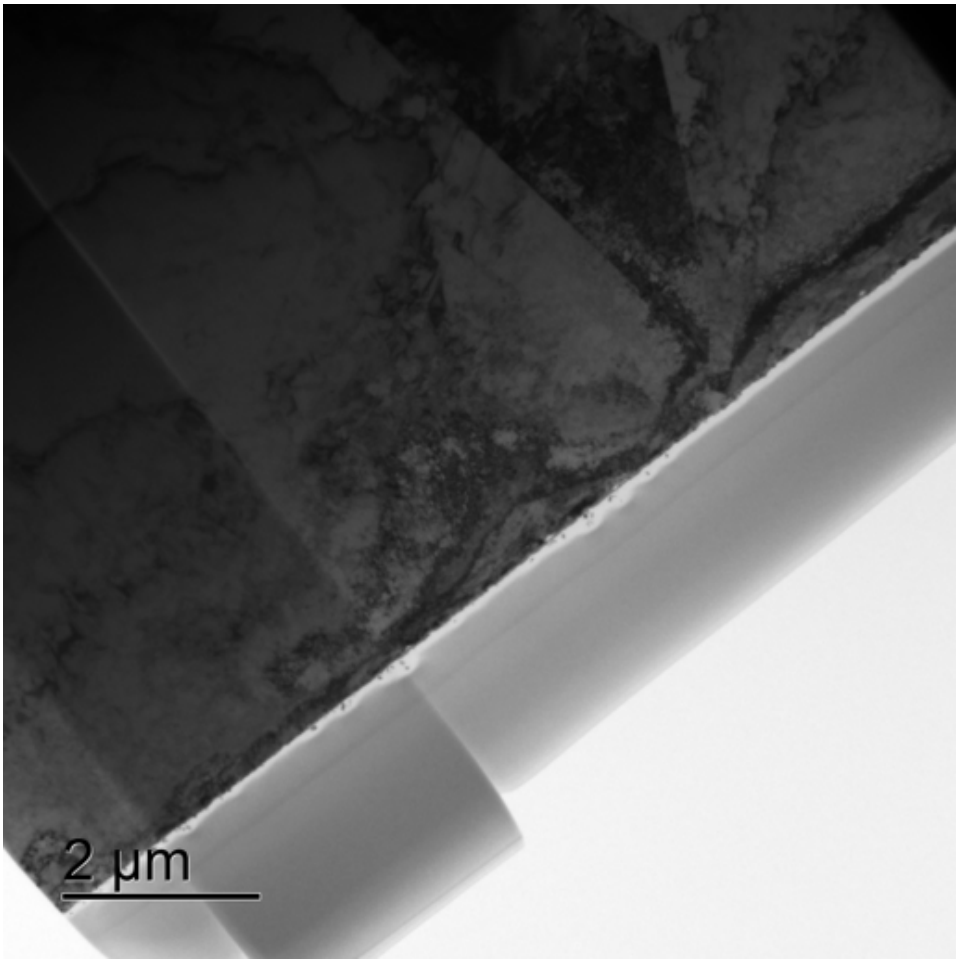

Figure 5.12: Bright Field TEM image of sample

shown in Figures 5.16 and 5.17. The thickness of the carbon layered on metal particles is approximately 4 nanometers, considerably less than in the high carbon coverage images.

The STEM mode of the microscope was used to develop EDS maps at two locations of the cross-section. The first location chosen was the grain boundary demarking the high and low carbon coverage regions. This location is shown in a BF image in Figure 5.18.

Figure 5.19 depicts the EDS map captured from this area. It can be seen that the region on the left-side of the grain boundary has a better-developed region of low chromium coverage

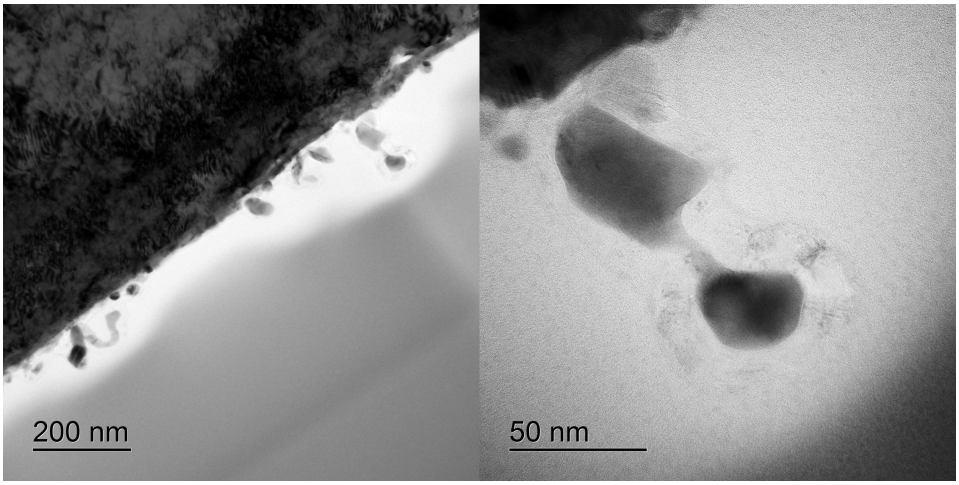

Figure 5.13: BF TEM image in region with higher observed carbon coverage. Metal particles separated from bulk material and surrounded by carbon filament.

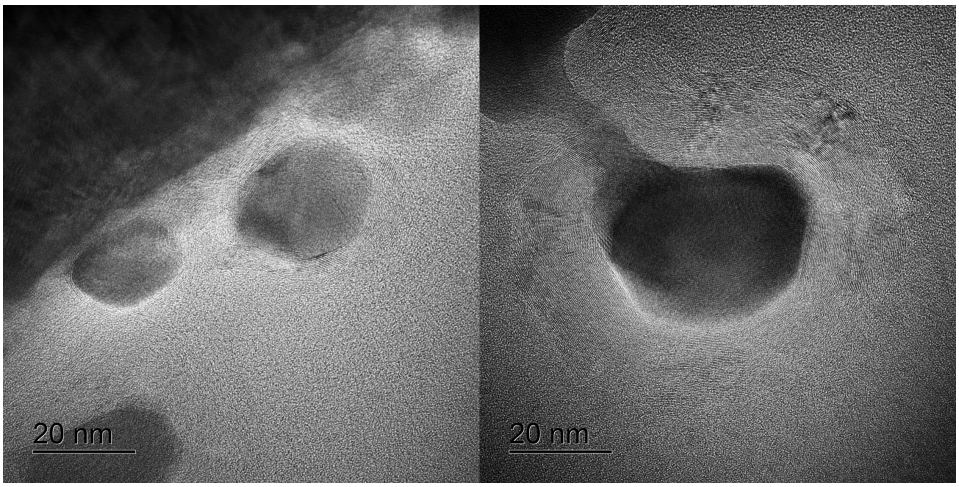

Figure 5.14: BF TEM image in region with higher observed carbon coverage. Metal particles separated from bulk material and surrounded by carbon filament.

below the surface (the magenta layer). In the low-carbon coverage region, chromium diffused more readily to the surface to form metal dusting resistant oxides. The area in the cyan box was selected to create a chart of relative abundance of iron, chromium, and nickel.

Figure 5.20 shows the relative abundance of the three most importance metal species go-

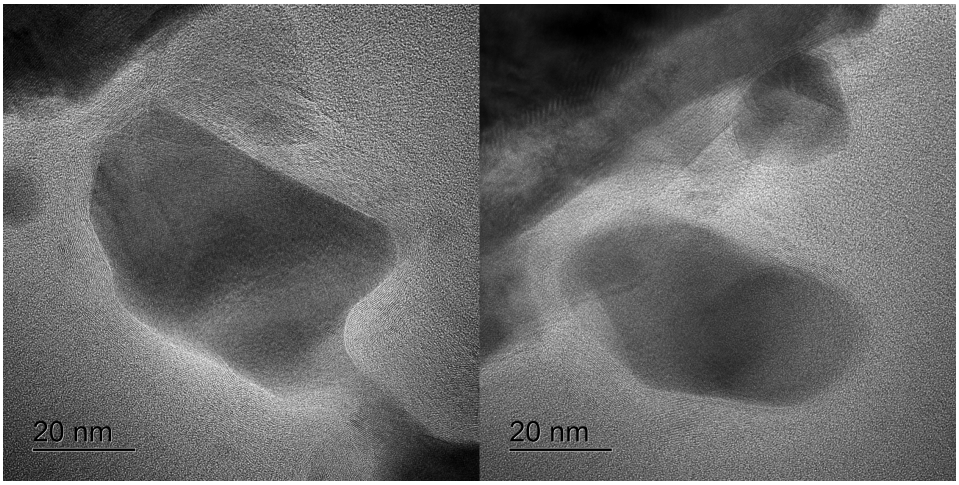

Figure 5.15: BF TEM image in region with higher observed carbon coverage. Metal particles separated from bulk material and surrounded by carbon filament.

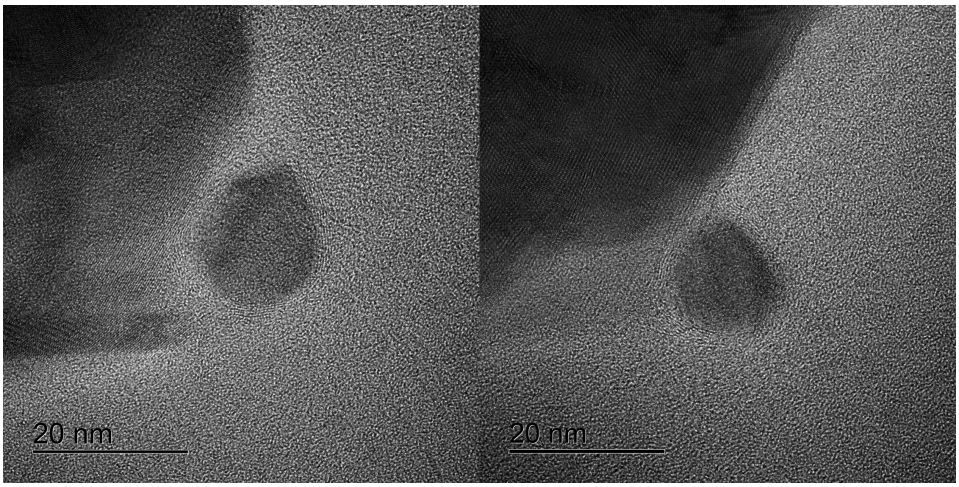

Figure 5.16: BF TEM image in region with lower observed carbon coverage.

ing into the material. It can be seen that the uppermost layer (the oxide) has higher relative abundance of chromium than the bulk. The sum of the relative abundances of iron, chromium, and nickel is approximately constant below the oxide layer at around 45%. Actual abundance is higher than this, as the previously given elemental make up of Incoloy 800 is >95% these three metals. It can also be seen from this chart that the oxide layer is approximately 40 nanometers thick in this area. Iron can be seen to be incorporated in

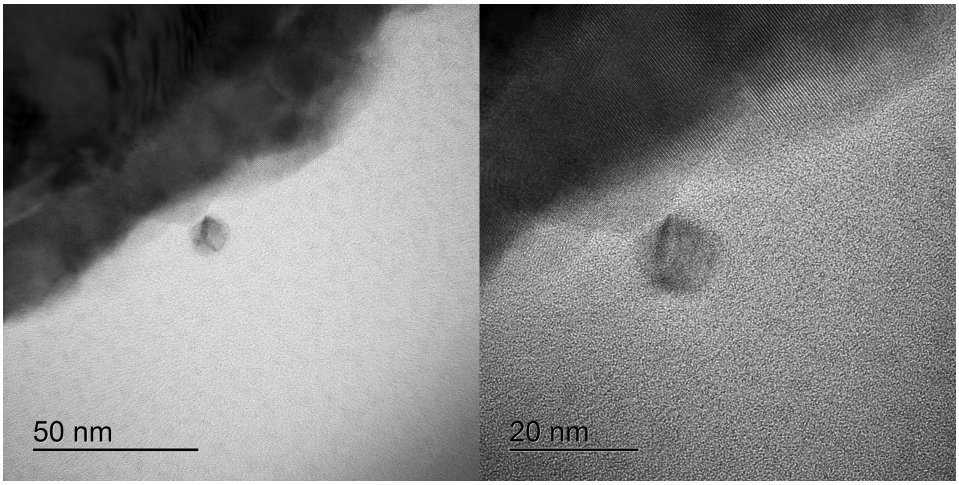

Figure 5.17: BF TEM image in region with lower observed carbon coverage.

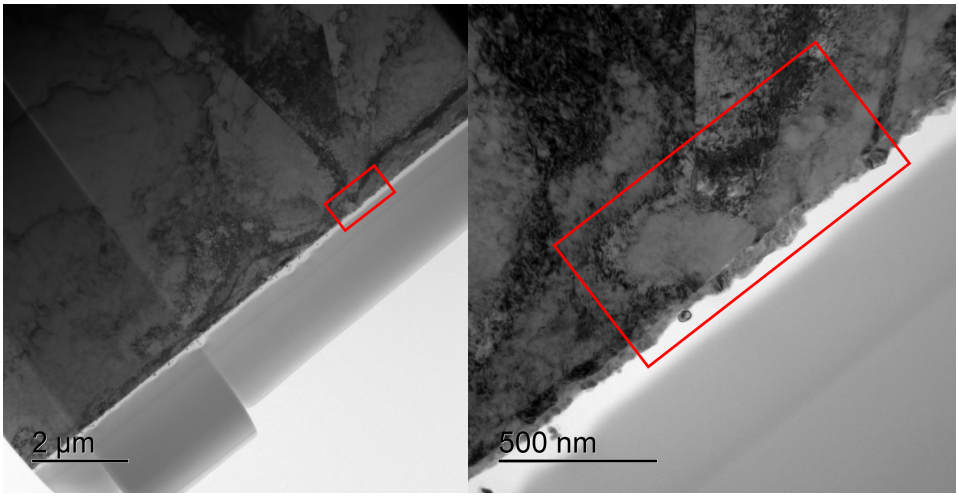

Figure 5.18: BF TEM image of location of EDS mapping at transition between high and low carbon coverage regions.

the oxide layer, while nickel is almost completely absent. It is likely that the oxides in this area are mostly chromium oxides (such as Cr_2O_3) and metal chromium oxides (such as $MnCr_2O_4$ and $FeCr_2O_4$) and spinels.

The location of the second EDS map is shown in Figure 5.21. This map, shown in Figure 5.22, is in the high-carbon coverage region of the sample, and was intended to capture

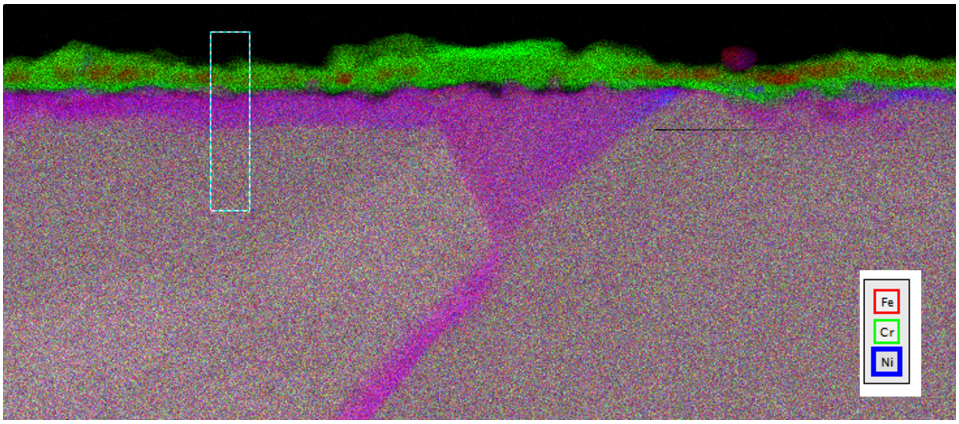

Figure 5.19: STEM EDS map at transition between high and low carbon coverage regions with iron, chromium, and nickel shown in RGB. The cyan box is approximately 200 nm tall.

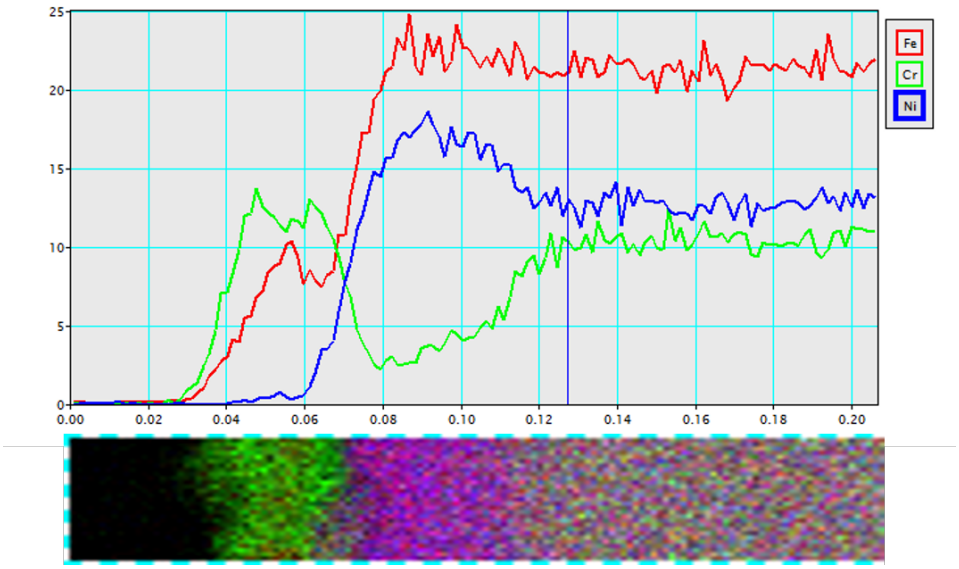

Figure 5.20: Relative abundance of iron, chromium, and nickel charted with sample depth on low carbon coverage side of sample, micrometers.

the make-up of the metal particles involve with carbon filamentation. A chart with the relative abundance of iron, nickel, and chromium in the region bounded by the cyan box is shown in Figure 5.23. Compared to the low-carbon coverage region, this area has a thinner oxide layer (about 20 nanometers compared to 40 nanometers in the low-coverage region) with relatively more chromium (15% compared to 12%) and less iron (5% compared to

9%). The magenta chromium-deficient region is also smaller in this region (only about 15 nanometers compared to 35 nanometers) and is less deficient in chromium.

The carbon-surrounded metal particle can be seen to be almost entirely iron, with a small amount of nickel. Most of the agglomerations in the larger EDS map can be seen to be iron-based and contain practically only iron, though there is one particle to the left of the cyan box that seems to be a blend of nickel and iron (blue and red).

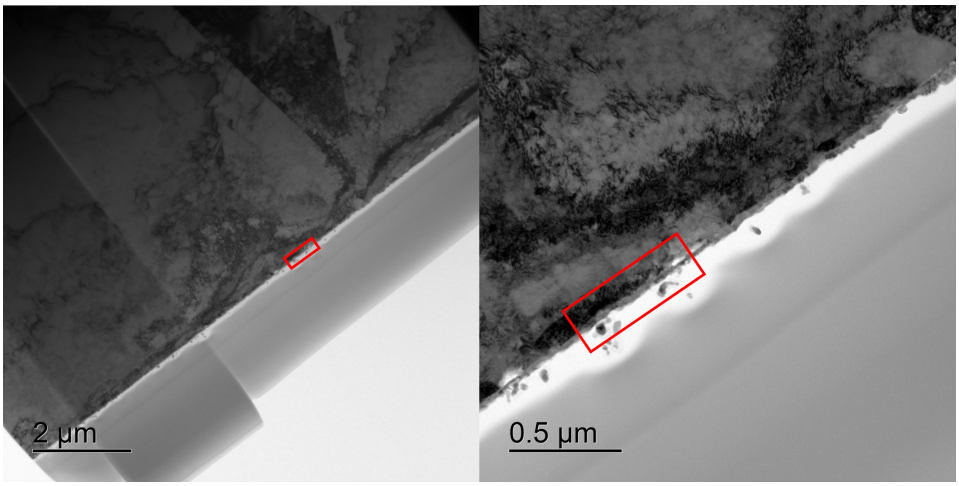

Figure 5.21: BF TEM image of location of EDS mapping at transition between high and low carbon coverage regions. Cyan box is approximately 200 nm

Selected Area Diffraction (SAD) patterns captured from the grains indicate a difference in grain orientation on either side of the interface between the high and low carbon coverage regions on the surface. These diffraction patterns are shown in Figure 5.24. The low carbon coverage side has low indices oriented toward the surface, while the high carbon coverage side has higher indices oriented toward the surface, which corresponds with the suggestion by Grabke that low-index orientations are more suited for chromium diffusion and oxide-scale formation [1].

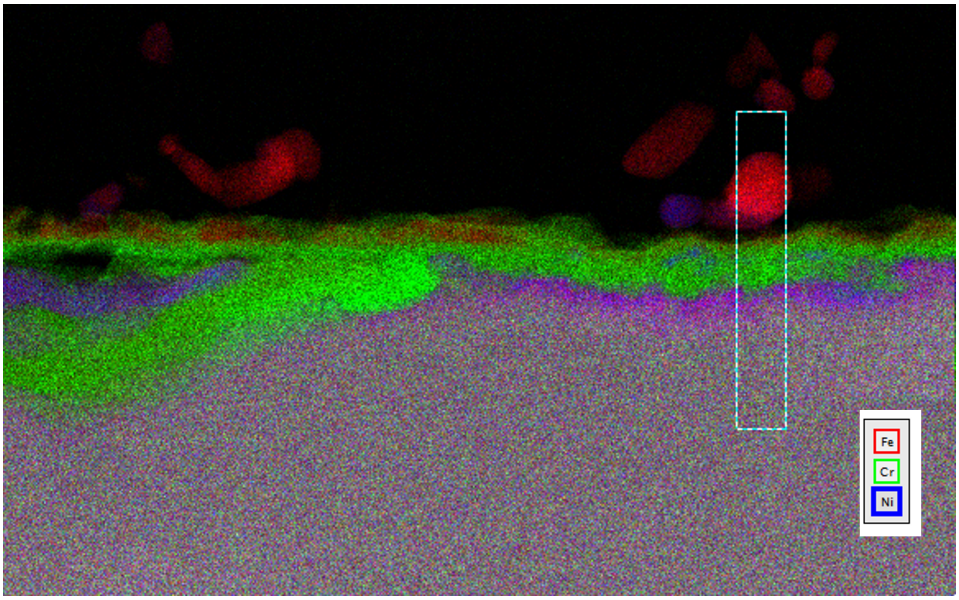

Figure 5.22: STEM EDS map of location of EDS mapping at transition between high and low carbon coverage regions with iron, nickel, and chromium shown in RGB

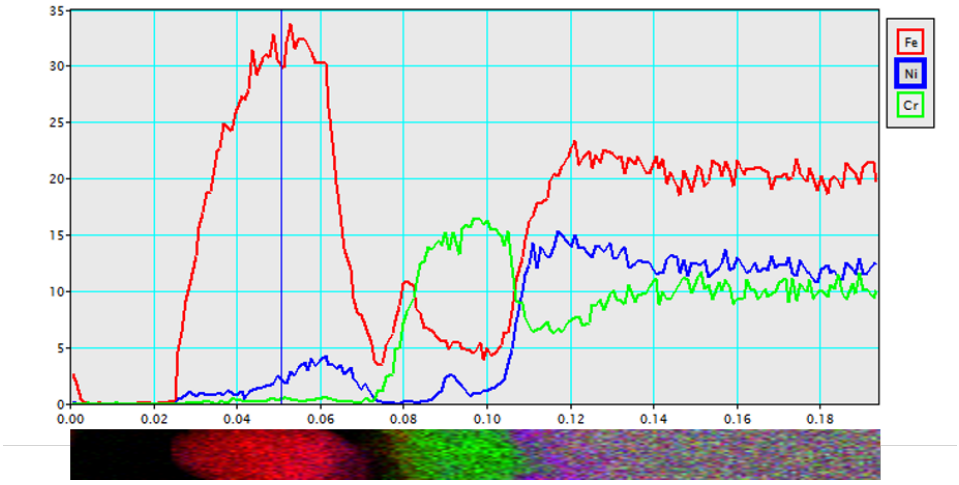

Figure 5.23: Relative abundance of iron, chromium, and nickel charted with sample depth on high carbon coverage side of sample, with detached catalyst particle

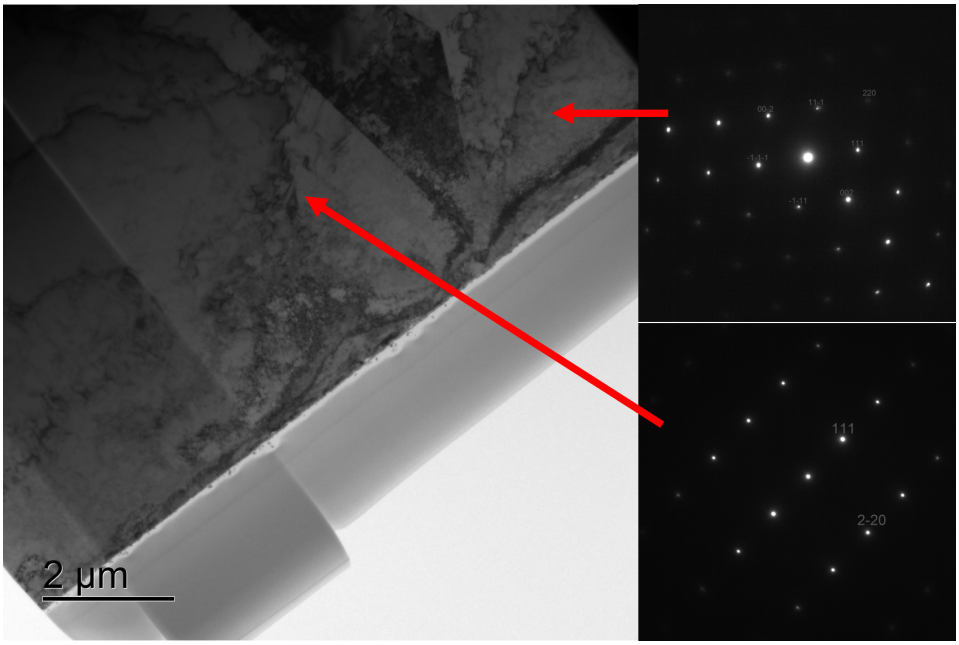

Figure 5.24: Selected Area Diffraction pattern showing difference in grain orientation on either side of high/low carbon coverage interface. The top diffraction pattern has Tx=-0.3, Ty=31.0. The bottom pattern has Tx=8.0, Ty=12.7

5.3.1 More Raman spectroscopy

It is possible to locate grains similar to those evaluated with TEM using the optical microscope attached to the Raman spectrometer. It has been previously described that tarnish color can be correlated with oxide composition [**?**]. One grain each of high and low carbon coverage on the 60 minute metal dusting condition Incoloy 800 sample was found and analyzed using Raman spectroscopy. The area of the sample where the TEM cross-section was removed was examined in order to find similar grains on another part of the sample to test. The two grains tested are shown in Figure 5.25. The two samples were normalized by their maximum value, which was the spinel peak appearing around 650 cm^{-1} for both areas. The low-coverage area seems to have slightly higher relative intensity of chromium containing oxide peaks (the peaks between 300 cm^{-1} and 500 cm^{-1}). The region identified as being higher carbon coverage shows carbon peaks with higher relative intensity, and the carbon seems to be more crystalline; a clear shoulder (D2) is present on the G peak

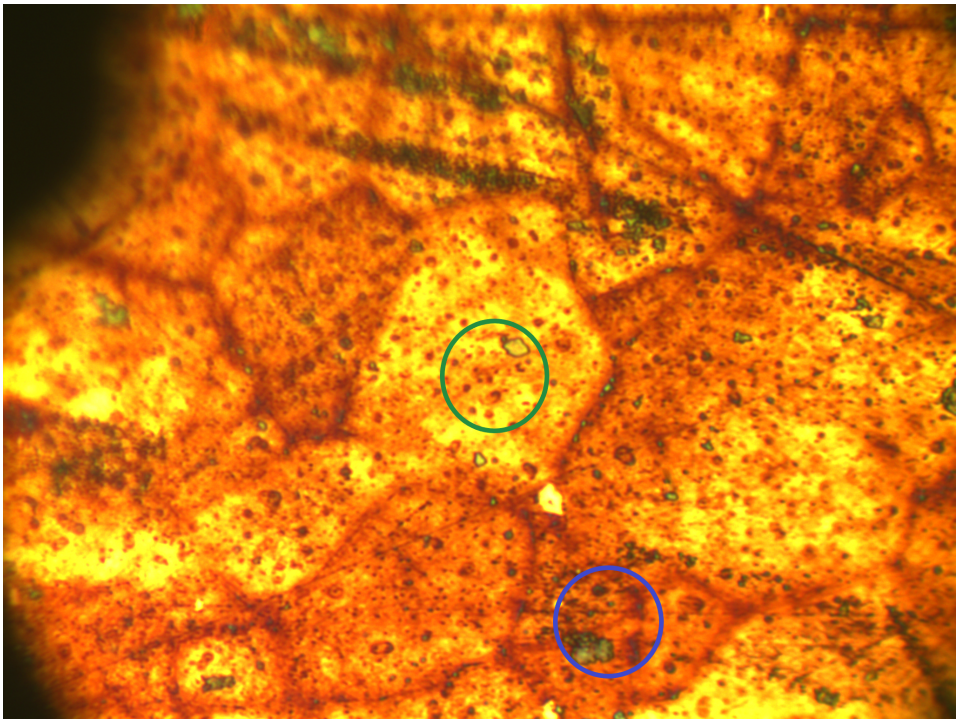

Figure 5.25: Optical micrograph of location of Raman spectroscopy in area analogous to area of TEM sample. Green: low carbon coverage region. Blue: high carbon coverage region.

occurring around 1600 cm^{-1}, whereas on the green, low-coverage grain the peak is wider with no apparent shoulder. Lack of a clear shoulder suggests the amplitude of the D2 peak is larger and makes up more of the total amplitude present in this peak. More graphitic carbon is associated with metal dusting corrosion 16.

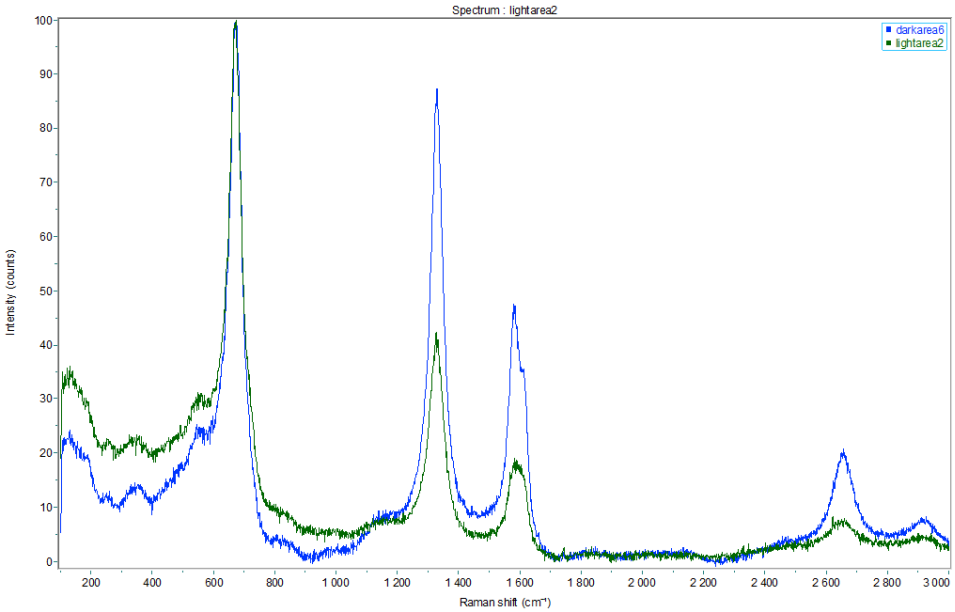

Figure 5.26: Plot of normalized Raman spectroscopy data corresponding with the colored circles in the previous figure, 100x magnification (green: low carbon coverage, blue: high carbon coverage)

Chapter 6

Conclusion and Further Work

Carbon filament formation was found on all sample wafers after being subjected to a metal dusting condition. In general, increasing metal dusting condition exposure time increases the perceivable amount of deposited carbon, although the 60 minute exposed Incoloy 800 sample had less coverage than the 20 minute exposed sample.

SEM characterization indicated that 601 wafers experienced extensive development of carbon filaments over the whole working wafer surface. The poor resistance of the 601 wafers to carbon deposition is likely due to the oxidation step not being aggressive enough to form a proper resistant oxide scale - a sample oxidized at a higher temperature showed enhanced oxide peaks in Raman spectroscopy. Grabke previously suggested that temperatures of 650°C and below might not consistently form an effective oxide scale [1].

Coverage was not as uniform on 800 wafers, but evidence of carbon deposition was found on all wafers. Variation in carbon coverage on 800 wafers could arise from variation in the pre-polishing of the wafers, which was done by hand. Effective polishing creates many dislocations and boundaries that can aid in diffusion of chromium to the surface of the alloy and the formation of a uniform oxide scale [1]. Insufficient or ineffective polishing could result in areas of poor diffusion.

Analysis with Raman spectroscopy suggests that carbon on the surface of the 601 wafers has higher crystallinity than that on the 800 wafers, but there was no obvious trend with different durations of the metal dusting step. The method used for peak deconvolution needs further evaluation, because small differences in found peak locations result in significant differences in peak amplitudes. Uncertainty should also be more effectively quantified.

An area on the 60 minute exposed Incoloy 800 sample was selected for TEM study. A difference in the amount of deposited carbon was identified on either side of a grain boundary. This difference was correlated with the development of a chromium-deficient layer and the oxide scale layer. A clearer, larger chromium-deficient layer and thicker oxide scale was associated with less carbon deposition on the surface. Selected Area Diffraction indicated a grain orientation difference between the regions, with the better chromium diffusion and oxide formation associated with lower indices oriented toward the surface. Low indices have previously been correlated with resistance to metal dusting [15].

Carbon on metal particles in the high coverage area was found to be much thicker than on those in the low coverage area. Metal particles seemed to be almost entirely iron particles, with a few iron/nickel composite particles. Analysis of the EELS maps generated was not attempted in this thesis, and much more information can be gleaned from the EDS data (e.g. examining relative compositions of species other than nickel, iron, and chromium).

Tarnish colors of the grains examined with TEM were matched to similar grains on the wafer, which were then analyzed with more Raman spectroscopy. A difference in the relative intensities of the carbon peaks was observed, with higher intensity peaks appearing on the grain similar to the high coverage carbon area examined with TEM. Carbon on the ”high-coverage” grain also exhibits higher crystallinity.

Further work is needed to better characterize the exact oxide compositions present in different regions and the conditions that promote resistant oxide scales. Raman spectroscopy is probably the most attractive tool to use for this analysis, as sample preparation is simple and analysis quick. TEM/STEM can provide a lot of data and interesting results, but the difficult sample preparation and small sampling area makes it difficult to produce statistical

or representative data. Raman spectroscopy could be used to compare relative intensities of oxide peaks that appear, but it may be more effective to perform this study on samples treated with a higher temperature oxidation step, as individual oxide peaks other than spinel were generally difficult to resolve on the samples oxidized at 540°C. Oxide peaks were much clearer on the 750°C oxidized sample.

Bibliography

[1] H. Grabke, "Thermodynamics, mechanisms, and kinetics of metal dusting," *Materials and Corrosion*, vol. 49, pp. 303–308, 1998.

[2] Z. Zeng, K. Natesan, and V. Maroni, "Investigation of metal dusting mechanisms in Fe-base alloys using Raman spectroscopy, x-ray diffraction, and electron microscopy," *Oxidation of metals*, vol. 58, pp. 147–170, 2002.

[3] Z. Zeng and K. Natesan, "Relationship between growth of carbon nanofilaments and metal dusting corrosion," *Chemistry of Materials*, vol. 17, pp. 3794–3801, 2005.

[4] J. Liu, B. Bao, H. Xu, B. Liu, and W. Zheng, "Inhibitory effect of MnCr2O4 spinel coating on coke formation during light naphtha thermal cracking," *Royal Society of Chemistry Advances*, vol. 6, pp. 68934–68941, 2016.

[5] N. Yao and Z. L. Wang, *Handbook of Microscopy for Nanotechnology*. Kluwer Academic Publishers, 2005.

[6] N. Tanaka, *Scanning Transmission Electron Microscopy of Nanomaterials: Basics of Imaging and Analysis*. Imperial College Press, 2014.

[7] B. Fultz and J. Howe, *Transmission Electron Microscopy and Diffractometry of Materials: Fourth Edition*. Springer, 2013.

[8] P. Larkin, *Infrared and Raman Spectroscopy: Principles and Spectral Interpretation*. Elsevier, 2011.

[9] K. Natesan and Z. Zeng, "Development of materials resistant to metal dusting degradation," tech. rep., Argonne National Laboratory, 2007.

[10] H. Grabke and M. Schutze, *Corrosion by carbon and nitrogen: metal dusting, carburisation and nitridation*. Woodhead Publishing Limited, 2007.

[11] P. Gunawardana, *Carbon formation phenomena and the initial stage of metal dusting corrosion - an experimental investigation*. PhD thesis, Norwegian University of Science and Technology (NTNU), 2014.

[12] Z. Zeng, K. Natesan, and M. Grimsditch, "Effect of oxide scale compositions on metal-dusting corrosion of Fe-based alloys," *Corrosion*, vol. 60, pp. 632–642, 2004.

[13] S. Strauss and H. Grabke, "Role of alloying elements in steels on metal dusting," *Materials and Corrosion*, vol. 49, pp. 321–327, 1998.

[14] X. Yang and S. Tu, "Stresses from oxide film imperfections during metal dusting," *Oxidation of metals*, vol. 78, pp. 295–305, 2012.

[15] D. Rohnert *et al.*, "Initial stages in the metal dusting process on alloy 800," *Oxidation of metals*, vol. 68, pp. 271–293, 2007.

[16] Z. Zeng and K. Natesan, "Relationship of carbon crystallization to the metal dusting mechanism of nickel," *Chemistry of Materials*, vol. 15, pp. 872–878, 2003.

[17] U. Poschl, R. Niessner, H. Grothe, H. Muckenhuber, and A. Sadezky, "Raman microspectroscopy of soot and related carbonaceous materials: spectral analysis and structural information," *Carbon*, vol. 43, pp. 1731–1742, 2005.

[18] "Inconel alloy 601." http://www.specialmetals.com/assets/smc/documents/alloys /inconel/inconel-alloy-601.pdf.

[19] "Incoloy alloy 800h and 800ht." http://www.specialmetals.com/assets/smc/documents/alloys /incoloy/incoloy-alloys-800h-800ht.pdf.

Appendix

6.1 Detailed process scheme

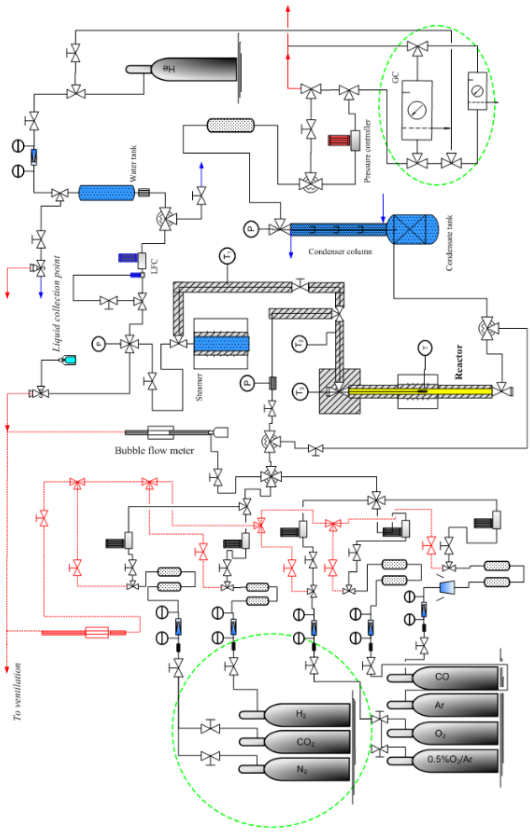

Figure 6.1: Detailed diagram of metal dusting experimental setup

6.2 Risk analysis

The project risk analysis report is included below.

ID	23702	**Status**	**Date**
Risk Area	Risikovurdering: Helse, miljø og sikkerhet (HMS)	Created	04.10.2017
Created by	John Theodore Helms	Assessment started	04.10.2017
Responsible	John Theodore Helms	Actions decided	
		Closed	

Risk Assessment:

CAT, Master student, 2017, John Theodore Helms

Valid from-to date:
10/4/2017 - 10/4/2020

Location:
K5 Hall D

Goal / purpose
Initial Stages of Metal Dusting Corrosion

Background
[Ingen registreringer]

Description and limitations

Prerequesites, assumptions and simplifications
[Ingen registreringer]

Attachments
[Ingen registreringer]

References
[Ingen registreringer]

Summary, result and final evaluation

The summary presents an overview of hazards and incidents, in addtition to risk result for each consequence area.

Hazard: **Acetone**

Incident:

Not to be analyzes.

Hazard: **Hexane**

Incident:

Not to be analyzes.

Hazard: **Carbon Monoxide (CO)**

Incident:

Not to be analyzes.

Hazard: **Falls**

Incident:

Not to be analyzes.

Hazard: **Heat/Burn risk**

Incident:

Not to be analyzes.

Hazard: **Argon**

Incident:

Not to be analyzes.

Hazard: **Solvent spills/splash**

Incident:

Not to be analyzes.

Hazard: **Pressure**

Incident:

Not to be analyzes.

Hazard: **Stop in Cooling**

Incident:

Not to be analyzes.

Hazard: **Electricity**

Incident:

Not to be analyzes.

Hazard: **Thermocouple loses contact with reactor**

Incident:

Not to be analyzes.

Final evaluation

Organizational units and people involved

A risk assessment may apply to one or more organizational units, and involve several people. These are lsited below.

Organizational units which this risk assessment applies to

- NTNU

Participants

Hilde Johnsen Venvik
Xiaoyang Guo
Karin Wiggen Dragsten

Readers

[Ingen registreringer]

Others involved/stakeholders

[Ingen registreringer]

The following accept criteria have been decided for the risk area Risikovurdering: Helse, miljø og sikkerhet (HMS):

Helse	Materielle verdier	Omdømme	Ytre miljø
☒	☒	☒	☒

Overview of existing relevant measures which have been taken into account

The table below presents existing measures which have been take into account when assessing the likelihood and consequence of relevant incidents.

Hazard	Incident	Measures taken into account

Existing relevant measures with descriptions:

PPE-Nitrile Gloves and Protective glasses
Nitrile gloves are used to avoid skin contact with solvents and residues left on process equipment.

Protective glasses are used to prevent chemicals from coming into contact with the eyes.

Fire Extinguishers
Fire extinguishers are present in Hall D.

Ventilation
Metal Dusting rig is ventilated to mitigate any unintended gas release

Gas Alarms
Gas alarms are installed in Hall D surrounding the rig to detect release of hazardous gases (e.g. CO).

Emergency Showers
Emergency Showers are present in Hall D in case of chemical exposure

Eyewash Stations
Emergency eyewash stations are present in Hall D in case of chemical contact with eyes.